Boron-pnictogens: Highly anisotropic two-dimensional semiconductors for nanoelectronics and optoelectronics

Mehmet Emin Kilic [*]

Computational Science Center, Korea Institute of Science and Technology, Seoul 136-791, Republic of Korea

Soheil Ershad Rad

UNAM-Institute of Materials Science and Nanotechnology, Bilkent University, Ankara 06800, Turkey

Semran Ipek

Department of Engineering Physics, Istanbul Medeniyet University, Goztepe 34700, Istanbul, Turkey

Seymur Jahangirov [†]

UNAM-Institute of Materials Science and Nanotechnology, Bilkent University, Ankara 06800, Turkey

Two-dimensional materials open up tremendous opportunities for nanoelectronics and optoelectronics. Using first-principles density functional methods, we predict a family of two-dimensional boron-pnictogen materials. Our results show that these materials have excellent energetic, dynamical, thermal, mechanical, and chemical stabilities. The intrinsic structural anisotropy found in these materials leads to highly direction-dependent mechanical, electronic, and optical properties. They possess highly anisotropic Young's modulus and Poisson's ratio. The tensile strength under uniaxial and biaxial deformations is found to be very high for these materials. Electronically, they are all semiconductors with narrow band gaps. The band gap energies can be tuned by alloying, strain engineering, and chemical functionalization. They exhibit anisotropic and high carrier mobility. All these electronic properties make them promising candidates for nanoelectronic device applications. Using state-of-the-art GW- Bethe-Salpeter equation approach, taking the electron-hole effect into account, the prominent optical absorption structure with strong anisotropy in the visible light region endow the boron-pnictogen materials with great potential in optoelectronics.

I. INTRODUCTION

The advent of graphene in 2004 can be considered as the genesis of the era of two-dimensional (2D) materials [1,2]. The outstanding properties found in graphene such as defectless ultrafast ballistic charge transport, ultrahigh strength, and very high surface to volume ratio motivated scientists to search for other 2D materials [3]. In general, the out-of-plane quantum confinement in a 2D structure can give rise to exotic features unprecedented in their bulk counterparts [4]. In graphene, the presence of Dirac cones induces a semimetallic nature. The absence of a band gap limits the applicability of graphene in semiconductor and optoelectronic technologies [5–7]. Many alternative 2D materials have been proposed to overcome these barriers [8]. However, the diversity of properties required in various fields of study demands an expansion in the database of 2D materials to offer materials with optimum efficiency for each application.

In contrast to carbon's conventional sp^2 and sp^3 orbital hybridization, its periodic table neighbor boron has a com-

plicated bonding behavior. Even the ground state electronic structure of boron is still unclear [9]. Borophene, a two-dimensional form of boron, has several allotropes, such as β_{12}, χ_3, striped, and graphene-like borophene, where individual boron atoms make from three to six bonds, depending on the geometry of the structure [10–13]. This bonding versatility of boron creates many possibilities for the design of novel 2D boron compounds with peculiar properties [14–17]. Among this family, hexagonal boron-pnictogens (h-BX, $X =$ N, P, As, and Sb) are the most studied and well-known ones. Although hexagonal boron nitride (h-BN) has a structure similar to graphene its electronic and thermal properties are different [18,19]. h-BN is an insulator with a band gap of $\sim$6 eV and it is more suitable for high-temperature applications [20]. For instance, h-BN can starts to oxidize at 700 °C while graphene starts to oxidize at 300 °C under the same condition [21,22]. Unlike h-BN, h-BP and h-BAs are not yet synthesized experimentally, but theoretically predicted to be thermodynamically stable. They have narrow direct band gaps (0.49–1.36 eV) with high carrier mobilities [23] which makes them a potential candidate for 2D nanoelectronic devices.

Going beyond conventional hexagonal sheets, tetrahexagonal structures (composed entirely of tetragonal and hexagonal atomic rings) as a new family of 2D materials are of

---
[*]mekilic@kist.re.kr
[†]seymur@unam.bilkent.edu.tr

current interest due to their novel anisotropic properties and broad applications [24–26]. For instance, tetrahexagonal carbides (*th-X*C_2, X = Si, Ge, Sn) with direct band gaps and excellent carrier mobilities have a great potential for nanoelectronics [27] while their pentagonal counterparts, obtained by Stone-Wales transformation, exhibit relatively large band gaps and strong optical absorption capability in the visible range, demonstrating their potential for photocatalytic water splitting applications [28]. Moreover, 2D tetrahexagonal BN (*th*-BN) has been recently discovered with robust stability and excellent anisotropic mechanical and electronic properties, including ultrahigh tensile strength, auxetic behavior, tunable band gap, and indirect-to-direct band gap transition and was suggested to be a suitable substrate for this family [29].

Searching for superior electronic and optical properties, we predicted a family of 2D boron-pnictogens using state-of-the-art first-principles methods. After optimizing the structural configuration through energy minimization, we assured that all structures satisfy the prerequisites of energetic, dynamic (vibrational), thermal, and mechanical stabilities, showing their high potential for synthesis. Then, to achieve an insight into the anisotropic mechanical behavior of these borides, we studied their most important strain-induced mechanical responses, including Young's modulus, Poisson's ratio, and ultimate tensile strength, all of which are of great importance for strain engineering of 2D materials. The electronic properties and their evolution under strain engineering were evaluated next. In the final section, their optical absorption behaviors were examined.

II. COMPUTATIONAL METHODS

We performed state-of-the-art first-principles calculations using the Vienna *Ab initio* Simulation Package (VASP) [30,31] based on density functional theory . Projector-augmented wave potentials [32] and the generalized gradient approximation with Perdew, Burke, and Ernzerhof (PBE) functional [33] were utilized to describe the exchange-correlation functional. A plane-wave basis set with an energy cutoff of 400 eV was employed. A $24 \times 24 \times 1$ Γ-centered k-point grid was used for Brillouin zone (BZ) integration. The structural configuration of atoms and lattice constants in equilibrium conditions were determined through minimization of the total energy using the conjugate gradient method until force components on each atom were reduced below 0.01 eV/Å. Periodic boundary conditions were applied along the x and y axis, and to create an artificial 2D condition, a vacuum spacing of at least 20 Å along the z axis was considered to prohibit any interaction between out-of-plane adjacent cells. The energy band gap underestimation, in the PBE scheme, was corrected using the Heyd-Scuseria-Ernzerhof hybrid functional (HSE06), constructed by mixing 25% of the nonlocal Fock exchange with 75% of the PBE exchange and 100% of the PBE correlation energy [34]. The dynamical stability was examined performing phonon dispersion calculations via the Phonopy package [35]. A $4 \times 4 \times 1$ supercell with a $2 \times 2 \times 1$ k mesh was adopted to calculate the atomic force and the dynamical matrix, with very high accuracy (the convergence criterion of the total energy was set to 10^{-8} eV).

To check the thermal stability, *ab initio* molecular dynamics (AIMD) calculations were performed under constant temperature (T) and volume (V), where the temperature was adjusted by a Nosé thermostat [36]. The AIMD simulations were performed for a duration of 6 ps with time steps of 1 fs. For optical absorption calculations, we employed the one-shot GW method (GW_0) together with solution of the Bethe-Salpeter equation (BSE) to account for electron-hole interactions [37–39]. Due to the computational limits, k-point sampling was limited to $8 \times 8 \times 1$, and the plane-wave cutoff energy was reduced to 350 eV, while the total number of bands was doubled.

III. RESULTS AND DISCUSSION

A. Atomic structures

The structural configuration of the 2D boron-pnictogen monolayers, abbreviated as *th*-BX (X = P, As, Sb, and $P_{0.67}As_{0.33}$), is presented in Figs. 1(a) and 1(b). The ordered sequence of tetragons and hexagons creates an orthorhombic unit cell with two unequal lattice constants of a and b, forming a *Pccm* symmetry (space group no 49). Categorized by the type of element and coordination number, the structure is composed of four distinct atomic sites, where for ease of reference, the three- and fourfold coordinated positions, occupied by boron (pnictogen) atoms are denoted by B^3 (X^3) and B^4 (X^4), respectively. From a side view angle, the structure consists of three atomic layers, where the middle layer made of B^4 and X^4 atoms is sandwiched between two layers made of B^3 and X^3 species. The structural thickness is defined as the vertical distance between these top and bottom layers. For comparison, thickness profile is divided into a thinner section between B^3 atoms, denoted by h_1 and thicker section between X^3 atoms, symbolized by h_2. Atomic bonds of B^3-X^3, B^3-X^4, and B^4-X^3 are identified by d_1, d_2, and d_3, respectively. The interbond angles are defined as θ_{1-6}. The numerical values of these structural properties are listed in Table I.

For *th*-BP, the lattice constants are found to be $a = 5.82$ Å and $b = 7.76$ Å, which are larger than those in *th*-BN ($a = 4.56$ Å and $b = 6.20$ Å) [29]. Likewise, we observed that the lattice constants show an expansion to reach $a = 6.14$ Å and $b = 8.12$ Å for *th*-BAs, and $a = 6.72$ Å and $b = 8.98$ Å for *th*-BSb as the atomic radius of the group-V elements increases. In all the *th*-BX compounds, the monolayer thickness along X^3 atoms is higher than B^3 atoms, and this difference gets more prominent as the atomic radius of X species increases, where h_1/h_2 ratio is 0.73, 0.71, 0.63, and 0.60 for *th*-BN, *th*-BP, *th*-BAs, and *th*-BSb, respectively. A similar trend exists between the bond lengths, where $d_3 > d_2 > d_1$, suggesting that B^3-X^3 bond (d_1) is stronger than the other two. Moreover, in both hexagonal and tetragonal building blocks, interbond angles with boron as the middle atom ($X^3-B^4-X^3$) are wider than their counterpart with X in the middle ($B^3-X^4-B^3$). In the *th*-BX compounds, the fourfold coordinated atoms resemble that of zinc-blende cubic BX (*c*-BX), and the threefold coordinated atoms are analogous to that of *h*-BX. Thus, the B^3-X^4 bond length in the *th*-BX compounds is almost equivalent to their *c*-BX counterparts,
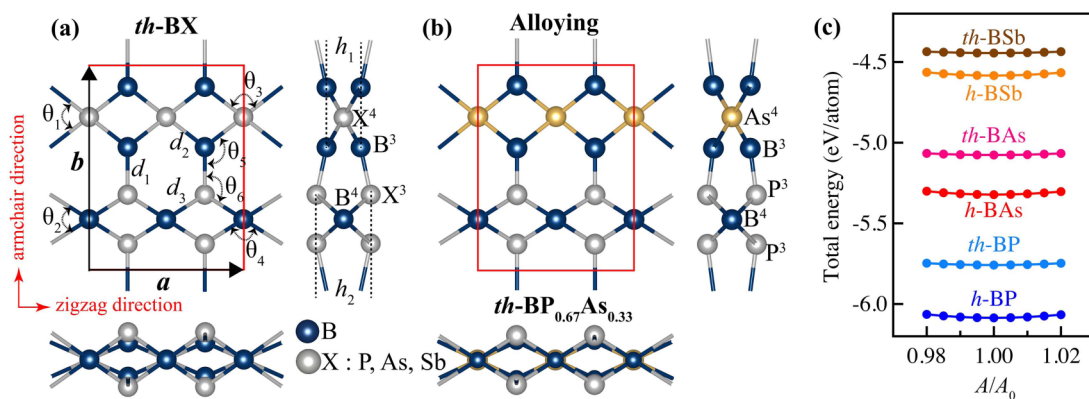
FIG. 1. Ball and stick model of (a) *th*-BX (X = P, As, and Sb) and (b) alloyed structure, from the top and side views. The unit cell is depicted in red line. Blue, gray, and orange balls represent B, X, and alloying element atoms, respectively. The d_1, d_2, and d_3 depict bond lengths; h_1 and h_2 represent buckling thicknesses. (c) Total energy of the *th*-BX structures with respect to their hexagonal counterparts (*h*-BX), where the minimum total energy is calculated in units of eV/atom around the equilibrium lattice area A_0.

where the B–X bond length is 1.96, 2.06, and 2.25 Å for *c*-BP [40], *c*-BAs [41], and *c*-BSb [42], respectively. The B^4−X^3 bonds, however, show an elongation compared to the B–X bond length in the *c*-BX structures, indicating weaker bonds in presence of threefold coordinated X species. Similarly, a comparison between the length of B^3−X^3 bonds in the *th*-BX compounds and that of their hexagonal counterparts with 1.85, 1.95, 2.15 Å [43], for B–P, B–As, and B–Sb, respectively, shows their compatibility. For *th*-BP$_{0.67}$As$_{0.33}$, the ball and stick model of the alloying structure is depicted in Fig. 1(b), where the alloying element (orange balls) substitute with the X^4 species. From Table I, it can be noted that the alloyed structure has the lattice parameters in between that of its nonalloyed parents. Likewise, the bond lengths of the alloyed structure show elongation compared to *th*-BP and shrinkage in comparison to *th*-BAs. Finally, it can be seen that due to the uneven distribution of the alloying element, the interbond angles does not follow the pattern found in the nonalloyed *th*-BX compounds.

We further calculated the electron localization function of the *th*-BX structures and presented in Fig. S1 of the Supplemental Material [44] found that there is a charge localization on the X atoms, which stems from the electronegativity difference between B and X elements (2.04, 2.19, 2.18, and 2.05 for B, P, As, and Sb, respectively). A high degree of electron localization at the middle of B–X bonds indicates the strong covalent bonding between B and X atoms in the *th*-BX structures.

In the following sections, we will see that this special configuration of tetragonal and hexagonal building blocks creates an intrinsic structural anisotropy, which is the main source of peculiar mechanical, electronic, and optical properties, found in the *th*-BX compounds.

B. Energetic stability

The relative energies of the *th*-BX compounds with respect to their hexagonal counterparts are presented in Fig. 1(c). It can be seen that as the atomic radius of the group-V element expands, the total energy of the structures decreases, in a way that each compound in tetrahex configuration has higher total energy compared to the hexagonal structure, showing the lower stability of these materials in tetrahex form. However, as the atomic number increases, the energy difference between tetrahex and hexagonal formations narrows. To gain a better insight into relative stability of the *th*-BX compounds, we further studied their cohesive energies (E_{coh}). Cohesive energy is the amount of energy required to overcome a crystals cohesion forces and decompose the structure into its constituent atoms, and it can be calculated, using the following formula:

$$E_{coh} = \frac{n_B E_B + n_X E_X - E_{BX}}{n_B + n_X},\qquad(1)$$

where E_B and E_X are the total energy of isolated boron and group-V element, respectively, and E_{BX} is the total energy of the *th*-BX compounds in the unit cell. The E_{coh} of the

TABLE I. Structural, energetic, and electronic properties of the *th*-BX compounds, where a and b are lattice parameters; h_1 and h_2 are the thicknesses; d_1, d_2, and d_3 are the bond lengths in unit of Å, $\theta_{(1-6)}$ are the inter-bond angles in unit of degree, E_{coh} is the cohesive energy in unit of eV/atom, E_g^{PBE}, E_g^{HSE}, $E_g^{GW_0}$ are the band gap energies obtained from PBE, HSE06, and GW_0 methods in unit of eV, respectively.

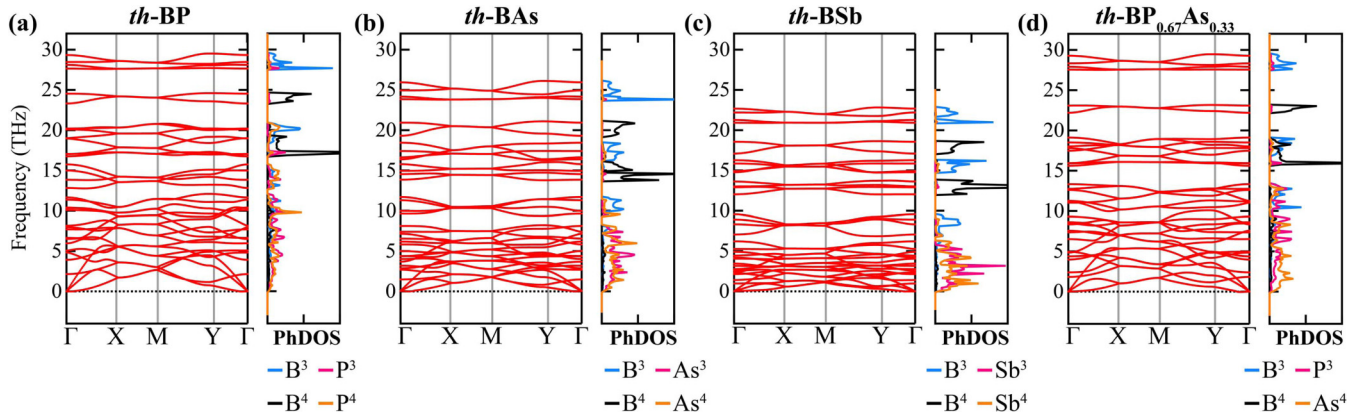| Structure	a	b	h_1	h_2	d_1	d_2	d_3	θ_1	θ_2	θ_3	θ_4	θ_5	θ_6	E_{coh}	E_g^{PBE}	E_g^{HSE}	$E_g^{GW_0}$
th-BN[a]	4.56	6.20	0.99	1.36	1.36	1.53	1.58	83.9	87.8	108.3	114.0	128.7	118.7	6.43	3.24	4.49	5.94
th-BP	5.82	7.76	1.32	1.86	1.81	1.95	1.98	83.4	85.5	110.0	121.3	128.1	114.4	4.68	0.43	0.94	1.31
th-BAs	6.14	8.12	1.36	2.17	1.93	2.06	2.12	83.8	87.1	109.1	125.2	129.5	110.1	4.09	0.29	0.75	1.08
th-BSb	6.72	8.98	1.44	2.41	2.15	2.26	2.33	83.9	87.7	108.1	125.3	130.1	109.3	3.59	0.04	0.38	0.71
th-BP$_{0.67}$As$_{0.33}$	5.99	7.88	1.41	1.88	1.80	2.05	2.01	85.9	83.4	108.1	123.6	128.8	114.1	4.45	0.70	1.27	1.56

[a]Reference [29].

FIG. 2. Phonon spectrum of the *th*-B*X* compounds, where the vibrational frequencies in the unit of THz are plotted versus the wave vector (*k*), along the high symmetry lines of the BZ.

th-B*X* compounds are listed in Table I. One can see that *th*-BN with 6.43 eV/atom has the strongest cohesive energy among this family. As the atomic radius of the *X* element increases, binding forces among the atoms deteriorate, reducing the cohesive energy in *th*-BP, *th*-BAs, and *th*-BSb to 4.68, 4.09, and 3.59 eV/atom, respectively. In case of the alloyed compound, the cohesive energy lies between that of the alloying components, where *th*-BP$_{0.67}$As$_{0.33}$ offers $E_{coh} = 4.45$ eV/atom, less than that of *th*-BP and superior to that of *th*-BAs. A comparison between the cohesive energies of the *th*-B*X* compounds and that of graphene with $E_{coh} = 7.94$ eV/atom [1], *th*-C with $E_{coh} = 7.12$ eV atom [24], *h*-BN with $E_{coh} = 8.82$ eV/atom [45], and *h*-BP with $E_{coh} = 6.15$ eV/atom [46] shows the inferior cohesion of the *th*-B*X* compounds. However, the aforementioned structures are among the most strongly bound 2D crystals, and the *th*-B*X* compounds have cohesive energies comparable to that of silicene with $E_{coh} = 4.70$ eV/atom [47], germanene with $E_{coh} = 4.15$ eV/atom [48], and phosphorene with $E_{coh} = 3.48$ eV/atom [49]. Although the cohesive energy value by themselves cannot verify the stability of a crystal, the fact that the *th*-B*X* compounds have cohesive energies in a range with several already synthesized 2D materials indicates that they are strongly bonded and have the potential to be synthesized.

C. Dynamical stability

Dynamical (vibrational) stability of the *th*-B*X* compounds was examined based on their phonon spectrum, presented in Fig. 2. Each atom in the unit cell has three vibrational degrees of freedom. The *th*-B*X* structures have 12 atoms in the unit cell and hence have 36 vibrational modes, three of which are acoustic, with zero frequency at Γ point, and the rest are optical modes. In a conventional 3D crystal, all of the acoustic modes have linear dispersion around the Γ point. In 2D materials, however, the out-of-plane acoustic branch has a quadratic dispersion, caused by the out-of-plane freedom of the 2D structure. According to the harmonic approximation, presence of imaginary frequencies within the vibrational modes is a manifestation of a disassembling force among the atoms, destroying the dynamical stability of a crystalline structure. Since no imaginary frequencies can be found in the

phonon spectrum of the *th*-B*X* compounds, their vibrational stability is guaranteed. Atom projected phonon density-of-states of each *th*-B*X* structure is presented next to its phonon spectra, in Fig. 2. In all of the compounds, the highest frequencies are related to the vibration of the B^3 atoms. The second-highest phonon frequencies are originated from the vibration modes of the B^4 atoms. There is a phonon gap between the vibrational modes of B^3 and B^4 atoms due to the different chemical-bond environments. The maximum of the vibrational frequencies and the phonon gap show a descending order as atomic radius of the *X* element increases, manifesting a similar trend in the bond strength. It is noted that the highest phonon frequencies in the *th*-B*X* compounds exceed those of *h*-BP, *h*-BAs, and *h*-BSb with ν_{max} of 29.0, 24.6, and 22.5 THz [43], respectively, revealing the greater robustness of the B−*X* bonds in tetrahex structures. Finally, one can see that the vibrational frequencies of the alloyed *th*-BP$_{0.67}$As$_{0.33}$ lie between that of *th*-BP and *th*-BAs.

D. Thermal stability

Thermal stability of the *th*-B*X* compounds was investigated through the AIMD simulations, performed at an elevated temperature for a duration of 6 ps. To provide a suitable condition for any possible rearrangement of the atoms, the AIMD simulations were performed in a 4×3×1 supercell. The diagrams of potential energy variation versus time, alongside the snapshots of the final atomic configuration after 6 ps were presented in Fig. S2 of the Supplemental Material [44]. The potential energies only have marginal fluctuations without any significant deviation from their mean value, suggesting that the structures are thermally stable at elevated temperatures and no structural reconfiguration is energetically favorable. The ultimate snapshots show that none of the bonds were broken at high temperatures and the overall skeleton of the structures remained intact after 6 ps. The maximum temperatures at which these observations held were 900, 800, 600, and 800 K for *th*-BP, *th*-BAs, *th*-BSb and the alloyed structure, respectively. Although computational cost limits the AIMD calculations to short time spans, in order of a few ps, these calculations can provide an insight into the response of the structure to a rapid temperature change, such as thermal shock.

TABLE II. Obtained mechanical properties of the *th*-BX compounds, where C_{ij} are the elastic stiffness constants in unit of N/m; Y_a and Y_b are Young's modulus in unit of N/m, ν_a and ν_b are the Poisson's ratios along zigzag and armchair directions, respectively; UTS$_a$, UTS$_b$, UTS$_{ab}$ are the ultimate tensile strains in % along zigzag, armchair and equibiaxial directions, respectively.

	Mechanical constants				Young's modulus		Poisson's ratio		Ultimate tensile strength		
	C_{11}	C_{22}	C_{12}	C_{66}	Y_a	Y_b	ν_a	ν_b	UTS$_a$	UTS$_b$	UTS$_{ab}$
th-BN[a]	232.46	195.49	4.17	73.41	232.39	195.40	0.02	0.02	32	36	27
th-BP	120.55	78.99	19.86	40.08	120.30	75.71	0.25	0.16	21	27	23
th-BAs	104.67	55.54	14.13	28.16	101.08	53.63	0.25	0.13	18	21	21
th-BSb	79.51	39.73	11.04	19.04	76.44	38.20	0.28	0.14	19	20	18
th-BP$_{0.67}$As$_{0.33}$	119.12	72.19	16.39	31.78	115.40	69.94	0.23	0.14	22	24	21

[a]Reference [29].

E. Mechanical stability

According to the Born-Huang elastic stability criteria [50], $C_{11}C_{22} - C_{12}^2 > 0$ and $C_{66} > 0$ are two prerequisites that need to be satisfied in a mechanically stable structure. Here C_{11}, C_{22}, C_{12}, and C_{66} are the elastic stiffness constants extracted from fitting the strain energy into the following function of the in-plane strains,

$$E_s(\varepsilon) = \tfrac{1}{2}C_{11}\varepsilon_x^2 + \tfrac{1}{2}C_{22}\varepsilon_y^2 + C_{12}\varepsilon_x\varepsilon_y + 2C_{66}\varepsilon_{xy}^2, \quad (2)$$

where E_s is the strain energy, ε_{xy} is the infinitesimal shear stress, and ε_x and ε_y are the infinitesimal uniaxial strains along the a and b lattice vectors, respectively. Different straining regimes can be used to calculate these elastic stiffness constants, where uniaxial strain along the x direction ($\varepsilon_y = \varepsilon_{xy} = 0$), uniaxial strain along the y direction ($\varepsilon_x = \varepsilon_{xy} = 0$), equibiaxial strain ($\varepsilon_x = \varepsilon_y$ and $\varepsilon_{xy} = 0$), and shear strain ($\varepsilon_x = \varepsilon_y = 0$) narrow down the Eq. (2) into the Eqs. (3), (4), (5), and (6) as follows, respectively:

$$E_s(\varepsilon) = \tfrac{1}{2}C_{11}\varepsilon_x^2, \quad (3)$$

$$E_s(\varepsilon) = \tfrac{1}{2}C_{22}\varepsilon_y^2, \quad (4)$$

$$E_s(\varepsilon) = \tfrac{1}{2}(C_{11} + C_{22} + 2C_{12})\varepsilon_x^2, \quad (5)$$

$$E_s(\varepsilon) = 2C_{66}\varepsilon_{xy}^2. \quad (6)$$

The variations in the strain energies of the *th*-BX compounds *vs* uniaxial, biaxial and shear strains are demonstrated in Fig. S3 of the Supplemental Material [44], where strains were applied in a range of −2 to 2% with an increment of 0.5%. These curves were fitted to the aforementioned system of equations to obtain the elastic stiffness constants, listed in Table II. One can see that the *th*-BX structures fulfill the Born-Huang elastic stability criteria as a guarantee to their mechanical stability.

F. Mechanical properties

Having secured the energetical, dynamical, thermal, and mechanical stability of all members of the *th*-BX family, we further studied in-plane Young's modulus (Y_{2D}), Poisson's ratio (ν), and ultimate tensile strength, as the most crucial mechanical properties in strain-engineering of 2D materials. We found that the intrinsic structural anisotropy induces highly direction dependent mechanical properties in the *th*-BX compounds. The following expressions were used to study the

evolution of Y_{2D} and ν as a function of the crystallographic orientation:

$$Y_{2D}(\theta) = \frac{C_{11}C_{22} - C_{12}^2}{C_{11}\sin^4\theta + A\sin^2\theta\cos^2\theta + C_{22}\cos^4\theta}, \quad (7)$$

$$\nu(\theta) = \frac{C_{12}\sin^4\theta - B\sin^2\theta\cos^2\theta + C_{12}\cos^4\theta}{C_{11}\sin^4\theta + A\sin^2\theta\cos^2\theta + C_{22}\cos^4\theta}, \quad (8)$$

where $A = (C_{11}C_{22} - C_{12}^2)/C_{66} - 2C_{12}$, $B = C_{11} + C_{22} - (C_{11}C_{22} - C_{12}^2)/C_{66}$, and θ is any arbitrary in-plane angle.

1. Young's modulus

The slope of the stress-strain curve within the elastic region defines the Young's modulus of a solid material. In other words, Young's modulus governs the deformation of a crystal under small strains, and thus is of great importance for strain engineering of a 2D material. The diagram of Young's modulus behavior as θ spans a whole 360° circle is shown in Fig. 3(a), where each color corresponds to a member of the *th*-BX family. It can be seen that the Young's moduli are highly direction dependent. In nonalloying members, the maximum and the minimum stiffness appear along the zigzag and the armchair directions of the crystal, respectively. For the alloying structure, the B–P bonds, which are oriented along the armchair direction, remain intact, making the Young's modulus of *th*-BP$_{0.67}$As$_{0.33}$ almost equivalent to that of *th*-BP. Along the zigzag direction, however, the Young's modulus obtains a value between that of *th*-BP and *th*-BAs. These results suggest that alloying is an effective approach to engineer the angle-dependent stiffness of the *th*-BX compounds. For the sake of comparison, the numerical values of the Young's modulus along zigzag and armchair directions, denoted as Y_a and Y_b, are listed in Table II. One can see that the stiffness values exhibit a descending order as the atomic radius of the X elements increases, which is compatible with previous vibrational results, showing the higher robustness of the shorter bonds. The maximum Young's modulus of the *th*-BP, *th*-BAs, and *th*-BSb structures, with Y_{max} equal to 120.30, 101.08, and 76.44 N/m, respectively, are comparable with that of the *h*-BP, *h*-BAs, and *h*-BSb structures, where Y_{max} are reported to be 141.9, 121.5, and 90.8 N/m [51], respectively.

2. Poisson's ratio

Another important strain-dependent mechanical response of a crystal is its Poisson's ratio (PR), the ratio between
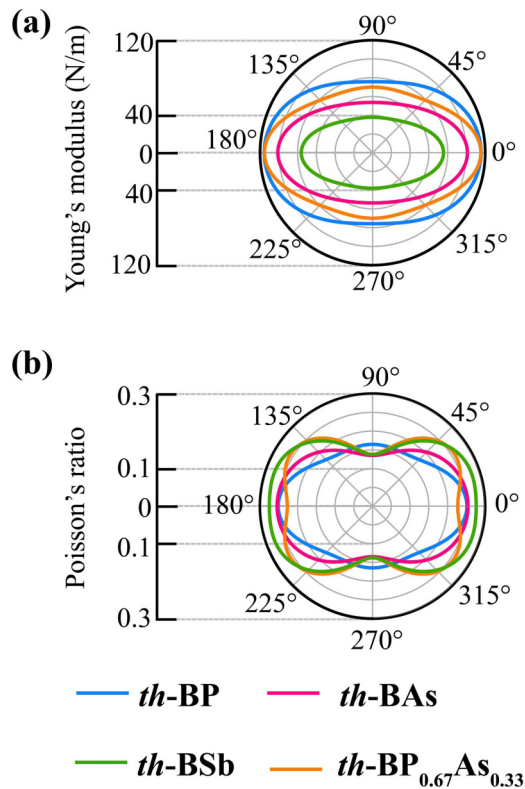
(a)

(b)

FIG. 3. Angle-dependent evolution of (a) Young's modulus (Y_θ) and (b) Poisson's ratio (ν_θ) in the *th*-BX structures.

the transverse strain and the strain along the direction of applied stress ($\nu = -\varepsilon_{\text{transverse}}/\varepsilon_{\text{axial}}$). The evolution of PR vs θ over a full 360° circle is depicted in Fig. 3(b), and the numeral value of PR along zigzag (ν_a) and armchair (ν_b) edges were reported in Table II. It can be seen that PR has also a significant angle dependence. The PR evolution in the *th*-BX structures resembles each other, with a maximum along zigzag and minimum along armchair direction. For the alloying structure, the highest PR value appears along the diagonal direction. Again, it can be seen that alloying can be employed to modify mechanical properties of the *th*-BX family and create features unprecedented in their unalloyed forms. Finally, it is noted that in spite of discovery of auxetic (negative PR) behavior in several tetrahexagonal structures [25,26,29], the *th*-BX compounds do not show auxetic behavior even under strain. To visualize the PR changes under strain, the transverse vs axial strain curves were shown in Fig. S4 of the Supplemental Material [44], where the slope of the curves shows the value of -ν. It can be noted that in all of the compounds and under any strain conditions, the slope of the curves remains negative, rendering a positive value for PR.

3. Ultimate tensile strength

During the strain engineering of a 2D material, extreme strains will be imposed into the crystal. In this condition, a suitable material for strain engineering should be able to maintain its integrity while deforming under strain. Ultimate tensile strength is the maximum stress tolerated by a crystal

right before its failure where the corresponding applied strain is defined as ultimate tensile strain (UTS). Thus, 2D materials with high ultimate tensile strength have a better potential for strain-engineering of their properties. To investigate the UTS of the *th*-BX compounds, a $2\times2\times1$ supercell was employed to measure the stress imposed into the system upon zigzag, armchair, and equibiaxial tensile strains. The obtained stress-strain curves are shown in Fig. 4, where the UTS points are depicted by dashed lines. The UTS values of *th*-BX compounds are reported in Table II. It can be seen that the UTS of the *th*-BX structures is also direction dependent. Similar to *th*-BN, in all compounds, UTS along the B^3-X^3 bonds (armchair direction) is higher than the zigzag direction. The UTS of *th*-BN is reported as 32%, 36%, and 27% along the zigzag, armchair, and biaxial directions, respectively [29]. For *th*-BP, the highest UTS among the *th*-BX compounds with 27% strain tolerance along the armchair direction. The UTS decreases as the atomic radius of the *X* elements expands to 21% and 20% for *th*-BAs and *th*-BSb, respectively, which is in agreement with the bond robustness trend, predicted from the phonon spectrum. It can be seen that *th*-BP$_{0.67}$As$_{0.33}$ shows a UTS of 22% along the zigzag direction, which is higher than that of *th*-BP and *th*-BAs as its parents. These results prove once more that alloying can be utilized systematically in the *th*-BX compounds to create properties unprecedented in the non-alloyed structures. Finally, a comparison between the UTS of the *th*-BX compounds, and graphene with a UTS of 27% [52] suggests that the boron-pnictogen monolayers with tetrahexagonal lattice can be categorized among 2D materials with ultrahigh UTS.

G. Electronic properties

The electronic properties of the *th*-BX compounds were calculated using PBE, HSE06, and GW_0 methods. The HSE06 electronic band structures, their corresponding projected density-of-states (pDOS), decomposed into orbitals and constituent elements, and the iso-surface of charge densities ($\rho = 0.005$ e/Å^3) for valence band maximum (VBM) and conduction band minimum (CBM) are presented in Fig. 5. We found that all members of the *th*-BX family are semiconductors with indirect narrow band gaps, except for *th*-BN. All the calculated band gap energy values from the PBE, HSE06, and GW_0 methods are given in Table I. It can be noted that in all the nonalloyed compounds VBM is close to the *M* point while the CBM is located at the *a*Y point in the BZ. After *th*-BN ($E_g = 4.49$ eV), *th*-BP has the widest band gap among *th*-BX compounds with $E_g = 0.94$ eV. As the atomic number of *X* element increases, the width of the band gap reduces to 0.75 and 0.38 eV for *th*-BAs and *th*-BSb, respectively. The *th*-BX compounds show a decrease in the band gap width and a direct to indirect transition compared to the electronic band structure of their hexagonal counterparts, which all have direct band gaps with $E_g = 1.37$, 1.18, and 0.61 eV for *h*-BP, *h*-BAs, and *h*-BSb [51], respectively. On the other hand, similar to the *th*-BX compounds, bulk zinc blende BX compounds (*c*-BX) have indirect band gaps. However, the band gap widths calculated using the local density approximation potential were reported to be higher than their tetrahex counterparts [41,42,53]. In compounds containing heavy elements such as
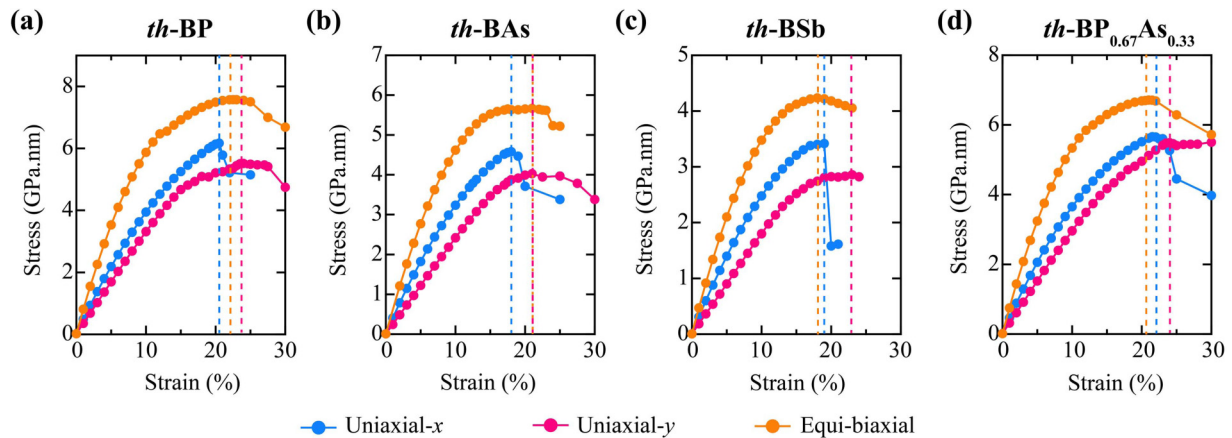
FIG. 4. Stress-strain curves for zigzag, armchair, and equi-biaxial tensile strains in the *th*-B*X* compounds, where the ultimate tensile strains (UTS) are denoted by dashed lines.

Sb, spin orbit coupling (SOC) can play an important role in the electronic behavior. Thus, the effect of SOC on the electronic band structure of *th*-BSb was investigated and demonstrated in Fig. S5 of the Supplemental Material [44]. It can be seen that although the SOC effect lifts the degeneracy of the bands, the width of the band gap decreases only slightly from 0.384 to 0.378 eV.

The pDOS plots have an overall similarity among all members, where the CBM is mainly made of p_z orbitals of the B^3, implying that states contributed by the B^3 species are responsible for the narrower band gap of the *th*-B*X* compounds compared to their hexagonal and zinc blende counterparts. In the case of the VBM, p_z orbitals are dominant too, but B^4 and X^3 species also contribute to VBM states in addition to B^3. Furthermore, it can be seen that in all nonalloyed structures, X^4 atoms have a negligible density of states near the valence and conduction band edges. The charge density distribution is also similar among nonalloyed compounds, where for VBM, the charge is mostly localized around the B^3, B^4, and X^3 atoms, and for CBM, the charge distribution is mainly concentrated around the B^3 species, in complete agreement with the pDOS results.

The alloyed *th*-BP$_{0.67}$As$_{0.33}$ compound electronic features, however, exhibit deviation from the nonalloyed compounds. It can be seen that due to alloying effect the VBM shifts to a point in the middle of the Γ-X edge of the BZ. Alloying increases the band gap energy to $E_g = 1.27$ eV, exceeding that of the *th*-BP and *th*-BAs, as its building parents. Moreover, the pDOS plots and charge density surfaces reveal that alloying reduces the density of B^4 states in VBM. These results suggest that alloying can be an effective approach for engineering the electronic properties of the *th*-B*X* compounds to fit the application at hand.

H. Strain engineering of the electronic properties

Previous studies have shown that strain engineering of the tetrahex structures can induce peculiar electronic behaviors such as semiconductor to metal transition, indirect-to-direct band gap transition, and wide band gap tunability [25–27,29,54,55]. Thus, after making sure that the *th*-B*X*

compounds are suitable candidates for strain engineering of their electronic properties, we investigated their electronic response to biaxial strain and uniaxial strains along zigzag (*x*) and armchair edges (*y*) ranging from −4 to 10% through the HSE06 method. The evolution of the band gap energies and band edges (CBM and VBM) vs strain is demonstrated in Fig. 6. It can be noted that the electronic behaviors of all structures under strain show similar trends. Generally, both tensile and compressive uniaxial-*x* strain tends to decrease the band gap energies. In the cases of biaxial and uniaxial-*y* strains, however, while compressive strain narrows the band gaps, tensile strain increases the band gap energies to a maximum around 6–8% strain, followed by a declining trend in higher values of tensile strain. A transition from semiconductor to metal can be found in the *th*-BSb structure upon 4% compressive biaxial strain. It can also be seen that although the alloyed structure has a band gap tunability similar to its constituent structures, its wider band gap compared to its parents is persistent under strain.

I. Effective mass and carrier mobility

To achieve a better insight into the electronic properties of the *th*-B*X* compounds, we further investigated the effective mass (m^*) and carrier mobility (μ). The effective mass was calculated by fitting a parabolic function into the VBM and CBM for holes and electrons, respectively, using the following expression:

$$m^* = \hbar^2 \left(\frac{d^2 E(k)}{dk^2} \right)^{-1},$$ (9)

where $\hbar$ is the reduced Planck constant, k is the wave-vector, and $\frac{d^2 E(k)}{dk^2}$ is the second derivative of the energy with respect to k. The calculated effective masses of electrons and holes, normalized with respect to the free electron mass (m_0), along the k_x and the k_y directions are given in Table III. We note that in all the *th*-B*X* compounds the effective masses are highly direction and carrier-type dependent. In particular, the ratios of electron effective masses in the k_y direction to those in the k_x direction are 4.79, 2.80, 3.71, and 4.33 for *th*-BP,
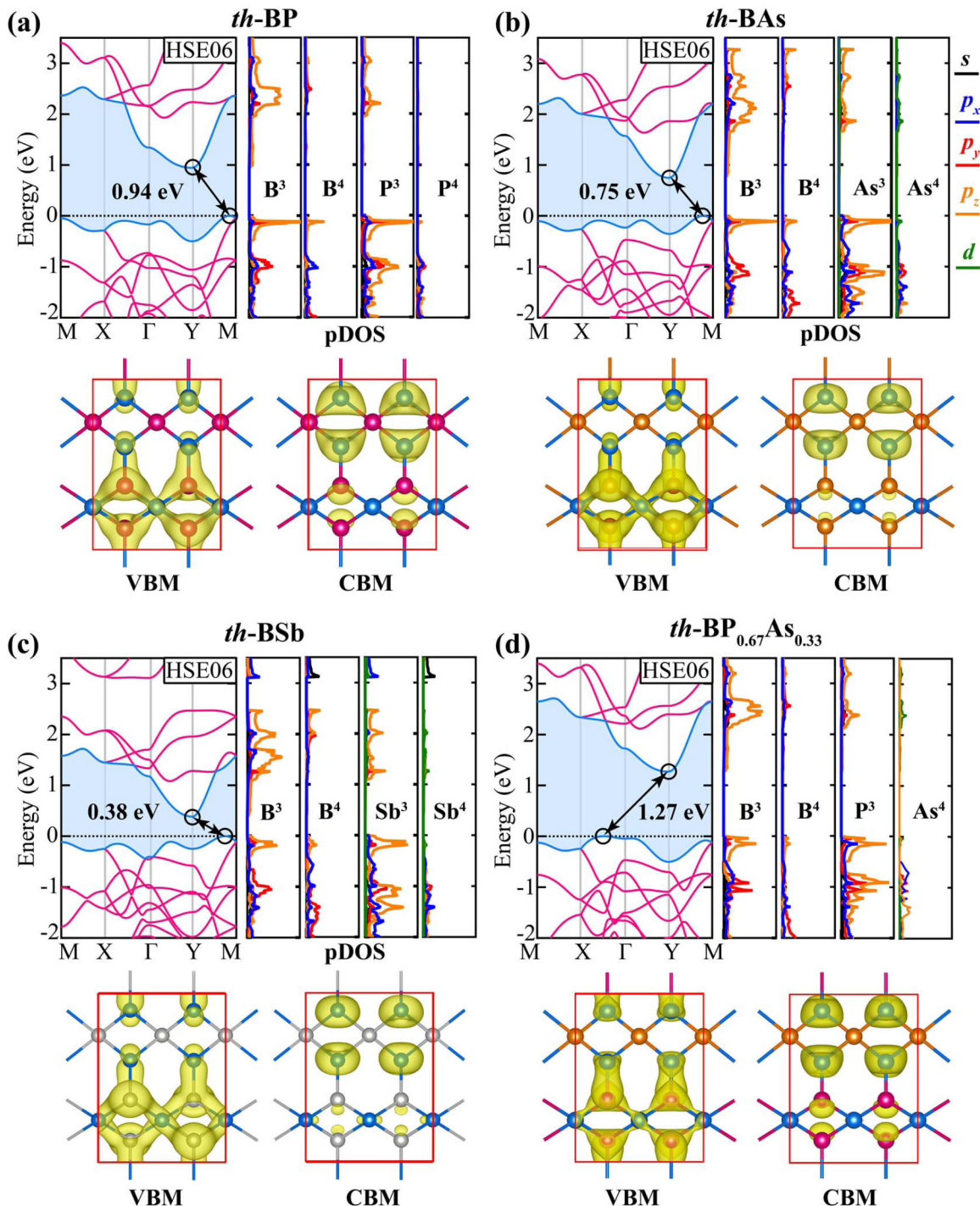
FIG. 5. Electronic band structure of the *th*-BX compounds obtained using HSE06 hybrid functional (top left panels). Double-headed arrows show the position of indirect band gaps between conduction band minimum (CBM) and valence band maximum (VBM). The Fermi level is set to zero and denoted by the dashed black line. The atomic and orbitally resolved projected density-of-states (pDOS) plots are presented next to their corresponding electronic band structure (top right panels). The bottom panels are the isosurfaces of charge density ($\rho = 0.005$ e/Å³) for VBM and CBM.

th-BAs, *th*-BSb, and the alloyed structures, respectively. This is in accordance with the charges projected to the conduction band edges shown in Fig. 5 which are dominated by the p_z orbitals of B³ atoms that form interacting chains along the zigzag direction leading to more dispersive bands. On the other hand, in the k_x direction the ratios of effective masses

of holes to those of electrons are 1.76, 2.60, 4.00, and 6.81 for the *th*-BP, *th*-BAs, *th*-BSb and the alloyed structures, respectively.

Having the effective masses, we further calculated the charge carrier mobilities along the k_x and the k_y directions (denoted by μ_x^{2D} and μ_y^{2D}, respectively) via Eq. (10) [56],
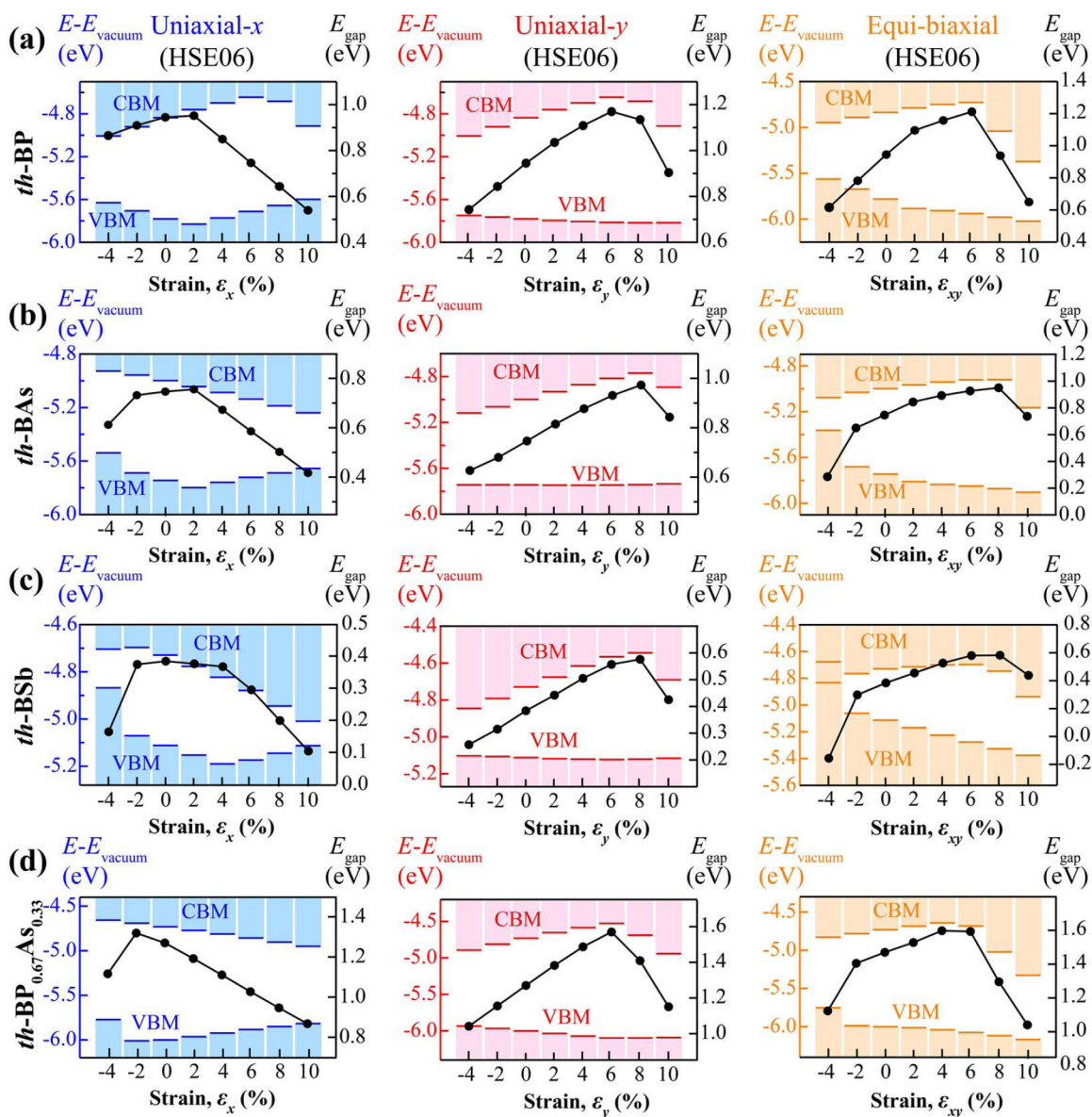
FIG. 6. Strain engineering of the electronic properties (band gap and band edges) of the *th*-B*X* compounds, calculated by HSE06 hybrid functional, for zigzag (uniaxial *x*), armchair (uniaxial), and biaxial strains within the range of −4% to 10% (negative/positive numbers correspond to the compressive/tensile strain), with increments of 2%. The black dots depict the band-gap values. The valence band maximum (VBM) and conduction band minimum (CBM) positions with respect to the vacuum energy are shown as bars.

which is a significant improvement over Eq. (11) [57] for anisotropic 2D materials:

$$\mu_i = \frac{e\hbar^3 \left(\frac{5C_i + 3C_j}{8} \right)}{k_B T (m_i^*)^{3/2} (m_j^*)^{1/2} \left(\frac{9E_{d,i}^2 + 7E_{d,i}E_{d,j} + 4E_{d,j}^2}{20} \right)}, \quad (10)$$

$$\mu_i = \frac{e\hbar^3 C_i}{k_B T m_i^* m_d E_{d,i}^2}. \quad (11)$$

Here m_i^* is the effective mass along the transport direction i and m_d is the geometric mean of the effective masses. Temperature is assumed to be $T = 300$ K. The $E_{d,i}$ is the deformation potential (DP) constant obtained from the following expression:

$$E_{d,i} = \frac{\Delta E}{\left(\frac{\Delta l}{l_0} \right)}, \quad (12)$$

where ΔE is the variation in the energy of the CBM and VBM bands under small uniaxial strains ranging from -1 to 1% with steps of 0.5% (see Figs. S6–S9 of the Supplemental Material [44]). The calculated DP constants of electron and hole for the *th*-B*X* compounds are summarized in Table III. It can be seen that the DP constants are also highly anisotropic. In all the compounds, the DP constant for electron along the armchair direction is higher than that along the zigzag directions whereas the DP for hole along the armchair direction is lower than that along the zigzag direction. The DP constant is correlated with the carrier-acoustic phonon interaction [58]. In

TABLE III. Charge carrier properties, where m_x^*/m_0 and m_y^*/m_0 are the carrier effective masses with respect to a static electron mass (m_0) along k_x and k_y directions, C_x^{2D} and C_y^{2D} are the elastic constants along zigzag and armchair directions in unit of N/m, $E_{d,x}$ and $E_{d,y}$ are the DP constants along zigzag and armchair directions in unit of eV, and μ_x^{2D} and μ_y^{2D} is the carrier mobility in unit of $\mathrm{cm^2 V^{-1} s^{-1}}$ at $T = 300$ K.

Structure	Carrier type	Effective mass		Elastic stiffness		DP constants		Carrier mobility	
		m_x^*/m_0	m_y^*/m_0	C_x^{2D}	C_y^{2D}	$E_{d,x}$	$E_{d,y}$	μ_x^{2D}	μ_y^{2D}
th-BP	Electron	0.29	1.39	120.55	78.99	1.79	4.32	1.54×10^3	0.19×10^3
	Hole	0.51	0.64	120.55	78.99	3.51	0.35	1.28×10^3	1.87×10^3
	Electron	0.20	0.56	104.67	55.54	2.06	3.38	4.14×10^3	1.00×10^3
	Hole	0.52	0.68	104.67	55.54	2.72	0.11	1.73×10^3	2.45×10^3
th-BSb	Electron	0.14	0.52	79.50	39.73	1.91	2.77	7.24×10^3	1.37×10^3
	Hole	0.56	0.47	79.50	39.73	2.08	0.27	2.22×10^3	4.41×10^3
th-BP$_{0.67}$As$_{0.33}$	Electron	0.27	1.17	119.12	72.19	1.87	3.88	2.00×10^3	0.29×10^3
	Hole	1.84	0.48	119.12	72.19	1.71	1.78	0.41×10^3	1.38×10^3

this respect, the stronger electron-acoustic-phonon interaction of the *th*-B*X* compounds along the armchair direction leads to a much larger DP constant than that along the zigzag direction. On the other hand, the holes are scattered more by acoustic phonons along the zigzag direction. The mobility depends on several anisotropic variables including the effective mass, DP constant, and elastic stiffness constants, which are listed in Table III. The calculated carrier mobilities of the *th*-B*X* compounds are on the order of 10^3 $\mathrm{cm^2 V^{-1} s^{-1}}$. They are highly direction-dependent and comparable or even higher than those of many 2D materials such as penta-CX_2 (X = P, As, Sn) ($\sim$310–9000 $\mathrm{cm^2 V^{-1} s^{-1}}$) [59], MoSSe (530 $\mathrm{cm^2 V^{-1} s^{-1}}$) [60], BN($\sim$487 $\mathrm{cm^2 V^{-1} s^{-1}}$). These highly anisotropic mobilities prolong the average charge carrier drift time, making these compounds suitable candidates for applications as photocatalyst by helping photoinduced pairs to engage in catalytic reactions before annihilation.

J. Optical absorption

To investigate the optical properties of the *th*-B*X* compounds, we calculated the complex frequency-dependent dielectric function ($\varepsilon(\omega) = \varepsilon_1 + i\varepsilon_2$). By employing the GW_0+BSE method, we obtained the optical spectra for two directions (zigzag and armchair) of polarization. Fig. 7 presents the evolution of ε_2 with respect to photon energy. The calculated GW_0 band gap (fundamental band gap) of *th*-BP, *th*-BAs, *th*-BSb, and *th*-BP$_{0.67}$As$_{0.33}$ is 1.31, 1.08, 0.71, and 1.56 eV, respectively, which are higher than those from the HSE functional. These fundamental band gaps are much smaller than the GW_0 gap in *th*-BN (about 5.94 eV). We note that both nonalloyed and alloyed structures offer highly anisotropic optical behavior, where the absorption along the armchair edge outweighs the zigzag edge. This direction-dependent optical response of the *th*-B*X* compounds can be exploited to manipulate the polarization of the incident beams and produce polarized light. Moreover, in all of the structures (independent of alloying effect), the greatest portion of the light absorption along the armchair edge occurs in the visible range. This is important, since visible light accounts for around 43% of the incident solar beams on the earth's surface. The prominent optical absorption of *th*-B*X* arises from the visible light region, promising for optoelectronic applications. For *th*-BAs, the prominent peaks are red-shifted to lower frequencies com-

pared to the *th*-BP due to its narrower band gap. Along the zigzag direction, the first optical absorption peak is observed in the infrared region while along the armchair direction it is in the visible region. Since *th*-BSb has the narrowest band gap compared to the rest of the compounds, it shows the most notable shift towards the infrared zone in its absorption along the armchair edge. Since alloying tends to widen the band gap, the absorption peaks in the alloyed structure show a shift towards the higher energies (blueshift). The apparent optical absorption with anisotropic response in the visible range make the *th*-B*X* compounds promising for optoelectronic applications.

K. Stability under oxidation

As many 2D materials exhibit very poor stability under ambient conditions, the chemical stability is of vital importance for their practical applications [61]. For instance, 2D black phosphorus with direct band gap is an excellent candidate for the optoelectronics applications. However, its applications are greatly limited due to its lack of enviromental stability
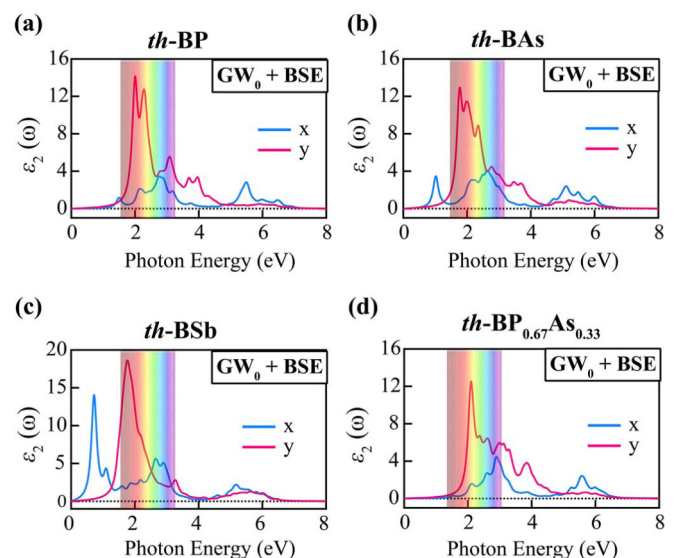

FIG. 7. The imaginary component of the dielectric function as a function of photon energy in the *th*-B*X* compounds along zigzag (x) and armchair (y) edges, calculated based on the GW_0+BSE method.
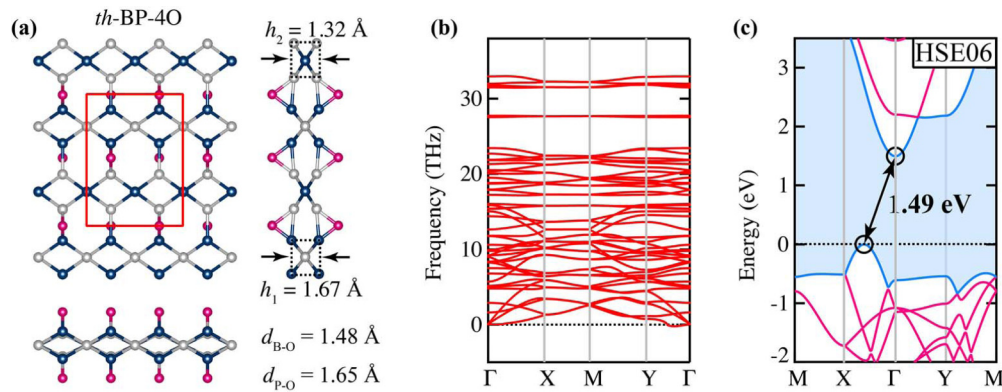
FIG. 8. (a) Top and side views of optimized atomic structure, (b) phonon dispersion curves, and (c) electronic band structure with HSE06 functional of O-*th*-BP. The unitcell is framed by red line inset. Blue, gray, and pink balls represent boron, phosphorus, and oxygen atoms, respectively. Fermi energy is set to 0 eV.

[62]. In this respect, we study the chemical stability of *th*-BP under oxidative environment as phosphorus is a light element compared to other group-V elements (As and Sb). To examine the oxidation mechanism, the adsorption of oxygen atoms on *th*-BP was investigated. We first studied a single oxygen atom adsorption on *th*-BP. To reveal the energetically favorable adsorption site, we placed the single O atom at different sites, including top sites (B^3-top, P^3-top, B^4-top, and P^4-top), bridge sites (B^3-P^3-bridge, B^3-P^4-bridge, and B^4-P^3-bridge), center of tetragon and hexagon, above a 2×2 supercell of the *th*-BP monolayer, depicted in Fig. S10 of the Supplemental Material [44]. Our calculations showed that the oxygen atom adsorbs preferentially on the B^3-P^3-bridge site with the adsorption energy of 3.02 eV, which is close to that on black phosphorus [63]. The high adsorption energy indicates strong chemisorption of the oxygen atom on *th*-BP. The bond length between the oxygen atom and B^3 (P^3) atom is 1.43 (1.70) Å. As presented in Fig. 5(a), the VBM of *th*-BP is mainly contributed by p_z orbitals of B^3-P^3 pairs, suggesting that the lone pair of B-P upper and lower layer bonds can be easily oxidized. Since oxidation reactions take place in an oxygen molecule (O_2) environment, we further studied adsorption of a single O_2 on *th*-BP. We noticed that upon structural optimization of the O_2 molecule placed on the fourfold coordinated atoms of *th*-BP, the molecule easily dissociates, and then the dissociated atoms are allocated to the nearest B^3-P^3-bridge sites (Fig. S10 of the Supplemental Material [44]). Next, we investigated full oxygen coverage of *th*-BP where oxygen atoms replaced the B^3-P^3-bridge site with double-sided configurations. The optimized atomic structure of the fully oxygenated *th*-BP monolayer is presented in Fig. 8(a). This structure is referred to as O-*th*-BP. The unit cell consists of four oxygen atoms. The thickness h_1 is increased from 1.32 to 1.67 whereas h_2 is decreased from 1.86 to 1.32 Å. Thus, the difference between h_1 and h_2 is reduced with full oxygen converage compared to that in *th*-BP. We further examine the dynamical stability of O-*th*-BP by calculating its phonon dispersion curve. As presented in Fig. 8(b) there is no imaginary frequency in the phonon spectrum. Verifying the dynamical stability of O-*th*-BP, we investigated the electronic properties by evaluating the electronic band structure and pDOS. The electronic band gap of O-*th*-BP is calculated as 1.49 eV,

which is 0.55 eV higher than that of *th*-BP monolayer. This shows that the band gap of *th*-B*X* compounds can be further tailored by the chemical functionalization as well as strain engineering.

IV. CONCLUSION

A comprehensive study on the stability, mechanical, electronic, and optical properties of a family of 2D boron-pnictogens (*th*-B*X* where X = P, As, Sb, and $P_{0.67}As_{0.33}$), based on first-principles methods was conducted. It was found that these materials have good energetic, vibrational, thermal, mechanical, and chemical stability, showing that they satisfy prerequisites for successful synthesis. Mechanical properties are highly anisotropic in these compounds, where Young's modulus along the zigzag edge is almost two times of that along the armchair edge. Poisson's ratio is also direction dependent with around 50% anisotropy between zigzag and armchair directions. These materials can tolerate ultrahigh tensile strains (up to 27% in the *th*-BP, comparable with UTS in graphene), making them suitable candidates for strain engineering of their properties. Electronic properties, calculated by the HSE06 functional, revealed the semiconducting nature of these compounds, where indirect band gaps in the range of 0.94 to 0.38 eV can be found in the nonalloyed structures. Moreover, highly anisotropic charge carrier effective mass and mobility were found, which prolongs the charge carrier drift time. The strong and anisotropic optical absorption in the visible range found in these compounds renders them as promising candidates for the optoelectronic applications. Combining this with the prolonged charge carrier migration creates an ideal condition for utilization of these materials as 2D photocatalysts. Additionally, it was found that strain engineering and alloying are two effective strategies for tailoring the properties of these compounds, where strain can be used to narrow the band gaps and alloying can be employed to widen the band gaps to higher than that of the nonalloyed materials. Moreover, mechanical properties can also be tuned by alloying to generate features unprecedented in the nonalloyed structures. Finally, we showed that the stability of *th*-BP monolayer is maintained even under an oxygen rich environment.

ACKNOWLEDGMENTS

[1] K. S. Novoselov, A. K. Geim, S. V. Morozov, D.-e. Jiang, Y. Zhang, S. V. Dubonos, I. V. Grigorieva, and A. A. Firsov, Science **306**, 666 (2004).

[2] K. S. Novoselov, A. K. Geim, S. V. Morozov, D. Jiang, M. I. Katsnelson, I. V. Grigorieva, S. V. Dubonos, and A. A. Firsov, Nature (London) **438**, 197 (2005).

[3] K. S. Novoselov and A. Geim, Nat. Mater. **6**, 720 (2007).

[4] S. Cahangirov, H. Sahin, G. Le Lay, and A. Rubio, *Introduction to the Physics of Silicene and other 2D Materials*, Vol. 930 (Springer, Berlin, 2016).

[5] P. R. Wallace, Phys. Rev. **71**, 622 (1947).

[6] F. Schwierz, Nat. Nanotechnol. **5**, 487 (2010).

[7] X. Li, J. Yu, S. Wageh, A. A. Al-Ghamdi, and J. Xie, Small **12**, 6640 (2016).

[8] S. Haastrup, M. Strange, M. Pandey, T. Deilmann, P. S. Schmidt, N. F. Hinsche, M. N. Gjerding, D. Torelli, P. M. Larsen, and A. C. Riis-Jensen, 2D Mater. **5**, 042002 (2018).

[9] X.-B. Li, S.-Y. Xie, H. Zheng, W. Q. Tian, and H.-B. Sun, Nanoscale **7**, 18863 (2015).

[10] B. Feng, J. Zhang, Q. Zhong, W. Li, S. Li, H. Li, P. Cheng, S. Meng, L. Chen, and K. Wu, Nat. Chem. **8**, 563 (2016).

[11] A. J. Mannix, X.-F. Zhou, B. Kiraly, J. D. Wood, D. Alducin, B. D. Myers, X. Liu, B. L. Fisher, U. Santiago, and J. R. Guest, Science **350**, 1513 (2015).

[12] W. Li, L. Kong, C. Chen, J. Gou, S. Sheng, W. Zhang, H. Li, L. Chen, P. Cheng, and K. Wu, Sci. Bull. **63**, 282 (2018).

[13] S. İpek, M. Kilic, A. Mogulkoc, S. Cahangirov, and E. Durgun, Phys. Rev. B **98**, 241408(R) (2018).

[14] H. Şahin, S. Cahangirov, M. Topsakal, E. Bekaroglu, E. Akturk, R. T. Senger, and S. Ciraci, Phys. Rev. B **80**, 155453 (2009).

[15] Rengin Peköz, M. Konuk, M. E. Kilic, and E. Durgun, ACS Omega **3**, 1815 (2018).

[16] S. Demirci, S. E. Rad, S. Kazak, S. Nezir, and S. Jahangirov, Phys. Rev. B **101**, 125408 (2020).

[17] S. Demirci, S. E. Rad, and S. Jahangirov, Phys. Rev. B **104**, 205432 (2021).

[18] Y. Kubota, K. Watanabe, O. Tsuda, and T. Taniguchi, Science **317**, 932 (2007).

[19] K. Zhang, Y. Feng, F. Wang, Z. Yang, and J. Wang, J. Mater. Chem. C **5**, 11992 (2017).

[20] G. Cassabois, P. Valvin, and B. Gil, Nat. Photonics **10**, 262 (2016).

[21] L. H. Li, J. Cervenka, K. Watanabe, T. Taniguchi, and Y. Chen, ACS Nano **8**, 1457 (2014).

[22] S. M. Kim, A. Hsu, M. H. Park, S. H. Chae, S. J. Yun, J. S. Lee, D.-H. Cho, W. Fang, C. Lee, T. Palacios *et al.*, Nat. Commun. **6**, 8662 (2015).

[23] M. Xie, S. Zhang, B. Cai, Z. Zhu, Y. Zou, and H. Zeng, Nanoscale **8**, 13407 (2016).

[24] B. Ram and H. Mizuseki, Carbon **137**, 266 (2018).

[25] M. E. Kilic and K.-R. Lee, Carbon **174**, 368 (2021).

[26] M. E. Kilic and K.-R. Lee, J. Mater. Chem. C **9**, 4971 (2021).

[27] M. E. Kilic and K.-R. Lee, Carbon **181**, 421 (2021).

[28] M. E. Kilic and K.-R. Lee, Phys. Rev. Materials **5**, 065404 (2021).

[29] M. E. Kilic and K.-R. Lee, Nanoscale **13**, 9303 (2021).

[30] G. Kresse and D. Joubert, Phys. Rev. B **59**, 1758 (1999).

[31] G. Kresse and J. Hafner, J. Phys.: Condens. Matter **6**, 8245 (1994).

[32] P. E. Blöchl, Phys. Rev. B **50**, 17953 (1994).

[33] J. P. Perdew, K. Burke, and M. Ernzerhof, Phys. Rev. Lett. **77**, 3865 (1996).

[34] J. Heyd, G. Scuseria, and M. Ernzerhof, J. Chem. Phys. **118**, 8207 (2003).

[35] L. Chaput, A. Togo, I. Tanaka, and G. Hug, Phys. Rev. B **84**, 094302 (2011).

[36] S. Nosé, J. Chem. Phys. **81**, 511 (1984).

[37] G. Onida, L. Reining, and A. Rubio, Rev. Mod. Phys. **74**, 601 (2002).

[38] S. Albrecht, L. Reining, R. Del Sole, and G. Onida, Phys. Rev. Lett. **80**, 4510 (1998).

[39] M. Rohlfing and S. G. Louie, Phys. Rev. Lett. **81**, 2312 (1998).

[40] P. Popper and T. A. Ingles, Nature (London) **179**, 1075 (1957).

[41] I. H. Nwigboji, Y. Malozovsky, L. Franklin, and D. Bagayoko, J. Appl. Phys. **120**, 145701 (2016).

[42] E. Deligoz, K. Colakoglu, and Y. O. Ciftci, J. Phys. Chem. Solids **68**, 482 (2007).

[43] C. Shi and X. Luo, arXiv:1811.05597 (2018).

[44] See Supplemental Material at http://link.aps.org/supplemental/10.1103/PhysRevMaterials.6.064007 for additional details on electron localization function; AIMD simulations for thermal stability; Strain energy vs strain for mechanical stability; Poisson's ratio; HSE06 electronic band structure of th-BSb with and without spin-orbit coupling; Deformation potential constants for the mobility; Optimized atomic structures of the oxygenated th-BP.

[45] M. Topsakal, E. Aktürk, and S. Ciraci, Phys. Rev. B **79**, 115442 (2009).

[46] M. M. Obeid, H. R. Jappor, K. Al-Marzoki, D. M. Hoat, T. V. Vu, S. J. Edrees, Z. M. Yaseen, and M. M. Shukur, Comput. Mater. Sci. **170**, 109201 (2019).

[47] N. D. Drummond, V. Zolyomi, and V. I. Falko, Phys. Rev. B **85**, 075423 (2012).

[48] S. Cahangirov, M. Topsakal, E. Aktürk, H. Şahin, and S. Ciraci, Phys. Rev. Lett. **102**, 236804 (2009).

[49] V. Vierimaa, A. V. Krasheninnikov, and H.-P. Komsa, Nanoscale **8**, 7949 (2016).

[50] M. Born and K. Huang, *Dynamical Theory of Crystal Lattices*, 1st ed. (Clarendon, London, 1954).

[51] Z. Zhou, H. Liu, D. Fan, and G. Cao, J. Phys.: Condens. Matter **31**, 385701 (2019).

[52] F. Liu, P. Ming, and J. Li, Phys. Rev. B **76**, 064120 (2007).

[53] J. I. Ejembi, I. H. Nwigboji, L. Franklin, Y. Malozovsky, G. L. Zhao, and D. Bagayokoa, J. Appl. Phys. **116**, 103711 (2014).

[54] M. E. Kilic and K.-R. Lee, Carbon **161**, 71 (2020).

[55] M. E. Kilic, S. E. Rad, and S. Jahangirov, Phys. Rev. Materials **6**, 035402 (2022).

[56] H. Lang, S. Zhang, and Z. Liu, Phys. Rev. B **94**, 235306 (2016).

[57] J. Bardeen and W. Shockley, Phys. Rev. **80**, 72 (1950).

[58] M. Long, L. Tang, D. Wang, Y. Li, and Z. Shuai, ACS Nano **5**, 2593 (2011).

[59] S. Sun, F. Meng, Y. Xu, J. He, Y. Ni, and H. Wang, J. Mater. Chem. A **7**, 7791 (2019).

[60] X. Ma, X. Wu, H. Wang, and Y. Wang, J. Mater. Chem. A **6**, 2295 (2018).

[61] J. Gao, B. Li, J. Tan, P. Chow, T.-M. Lu, and N. Koratkar, ACS Nano **10**, 2628 (2016).

[62] J. O. Island, G. A. Steele, H. S. van der Zant, and A. Castellanos-Gomez, 2D Mater. **2**, 011002 (2015).

[63] Q. Li, Q. Zhou, L. Shi, Q. Chen, and J. Wang, J. Mater. Chem. A **7**, 4291 (2019).